Integrated Approaches to Non-Rigid Registration in Medical Images

Yongmei Wang* and Lawrence H. Staib*+

Departments of Electrical Engineering* and Diagnostic Radiology+
Yale University, P.O. Box 208042, New Haven, CT 06520-8042
Email: wang@noodle.med.yale.edu, lawrence.staib@yale.edu

Abstract

This paper describes two new atlas-based methods of 2D single modality non-rigid registration using the combined power of physical and statistical shape models. The transformations are constrained to be consistent with the physical properties of deformable elastic solids in the first method and those of viscous fluids in the second to maintain smoothness and continuity. A Bayesian formulation, based on each physical model, on an intensity similarity measure, and on statistical shape information embedded in corresponding boundary points, is employed to derive more accurate and robust approaches to non-rigid registration. A dense set of forces arises from the intensity similarity measure to accommodate complex anatomical details. A sparse set of forces constrains consistency with statistical shape models derived from a training set. A number of experiments were performed on both synthetic and real medical images of the brain and heart to evaluate the approaches. It is shown that statistical boundary shape information significantly augments and improves physical model based non-rigid registration and the two methods we present each have advantages under different conditions.

1 Introduction

Comparing function or morphology between individuals requires non-rigid registration, because the detailed anatomical structure differs, sometimes greatly, between individuals. The goal of our non-rigid registration is to remove structural variation between individuals by matching an atlas image to each individual, or study, image, in order to have a common coordinate system for comparison. Shape differences between the atlas and study's anatomy are contained in the non-rigid transformation.

There have been many approaches to non-rigid registration in recent years [2, 3, 6, 7, 8, 11]. Usually, the transformation is constrained in some way because of the ill-posedness (i.e. in this case, the existence of many possible solutions) of the problem. Physical models, for example, linear elastic and viscous fluid models, are widely used to enforce topological properties on the deformation and constrain the enormous solution space [3, 4, 6, 7, 8]. Here, we are particularly interested in intensity based deformation using elastic or fluid models. Our goal is to incorporate statistical shape information into this type of physical model based registration and to develop a more accurate and robust algorithm.

Christensen *et al.* [3] present two physical models for non-rigid registration of the brain. The transformations are constrained to be consistent with an elastic model in the first method and a fluid model in the second. The elastic model requires less computation compared to the fluid model and penalizes deformation in proportion to the deformed distance. This is often too strict a model because of the large variation between anatomical structures and does not allow for the complete deformation necessary. Viscous fluid models are less constraining than elastic models and allow long-distance, nonlinear deformations of small subregions (Figure 1 top). However, no matter what model is used, elastic solid [8], viscous fluid [4], or other physics model such as hyperelasticity [9], in these cases, the deformed configuration of the atlas is always determined by driving the deformation using only pixel-by-pixel intensity difference between images. In many applications, however, this kind of warping is under-constrained and admits to unreasonable registration. Corresponding anatomical structure may shift or twist away from one position to another, and very large volumes of matter may stream through very small areas from one region to another (Figure 2(a)(b)). Even if the driving force is very small, the transformation may not be accurate enough, or may even be completely wrong, *even though* the deformed atlas and study appear similar (Figure 2(b)(c)(d)). In these circumstances, if shape information embedded in corresponding boundary points (Figure 2(e)(f)) had been included, the correct mapping or registration could have been found (Figure 2(g)(h)). In addition,

due to the use of the gray-level gradient of the deformed atlas in the body force formulation [3], lower contrast objects deform much slower than high-contrast objects, independent of their importance. Sometimes objects do not deform correctly because their gradient is too low compared to high-gradient objects and the smoothness ensured by the physical models dominates the whole deformation (Figure 1(d)). With the incorporation of the shape information embedded in corresponding boundary points (Figure 1(e)(f)), the result is improved (Figure 1(g)).

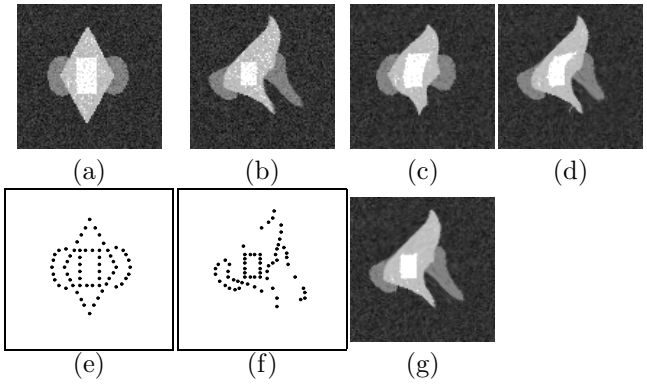

Figure 1: Comparison of synthetic image (100 × 100) non-rigid registration. (a): atlas image; (b): study image; (c): final deformed atlas by Christensen&Miller's elastic model [3, 8], showing large distance deformations prevented using the appropriate elasticity parameter to just ensure a globally positive Jacobian; (d): final deformed atlas by Christensen's fluid model [4], showing that large deformations can be accommodated (compare to (c)), but the shape of the brightest object (rectangular) is not maintained (compare to (g)); (e): atlas image control points; (f): study image control points; (g): final deformed atlas using our viscous-fluid mapping, showing appropriate deformation (compare to (d)).

Davatzikos and Prince [6] propose a method that deforms the boundaries in one image into those in another image based on a one-to-one mapping they established. The rest of the image is deformed by solving the equations describing the deformation of an elastic body using the boundary deformation as input. In this approach, although the mapping may be accurate on the boundary, the farther away the structure is from the boundary, the more error there is, because only information from object boundaries is used for registration. In addition, the boundary information used in their approach is derived by an active contour algorithm [6] which does not guarantee true correspondence, and it does not include any shape information which we believe is crucial in non-rigid registration for medical images.

2 Physical Models

We use analogous physical models to enforce topological properties on the deformation. An Eulerian reference is used in our physical model formulation. In this frame, a particle is tracked with respect to its final coordinates. The non-rigid registration is defined by the transformation corresponding to a homeomorphic mapping of the coordinate system, defined in 2D by:

$$\vec{w} = (x, y) \rightarrow (x - u_x(\vec{w}), y - u_y(\vec{w})) \qquad (1)$$

where $\vec{u}(\vec{w}) = [u_x(\vec{w}), u_y(\vec{w})]^T$ is the displacement at each pixel $\vec{w}$ whose coordinate is denoted as (x, y). A necessary condition for a transformation to be homeomorphic is that its Jacobian is globally positive. This mapping allows for the detailed local transformation into the specific anatomy of the individual, or study. We want to find the transformation that best matches the atlas with the study, constrained by the physical models. The following formulations of the physical models are similar to that in [3].

2.1 Elastic Model

For linear elastic solids, the force is proportional to the displacement. The spatial transformation satisfies the partial differential equation (PDE):

$$\mu\nabla^2\vec{u} + (\mu + \beta)\vec{\nabla}(\vec{\nabla} \cdot \vec{u}) = \vec{F}(\vec{u}) \qquad (2)$$

with certain boundary conditions such as that $\vec{u}(\vec{w}) = 0$ for $\vec{w}$ on the image boundary. In this equation, μ

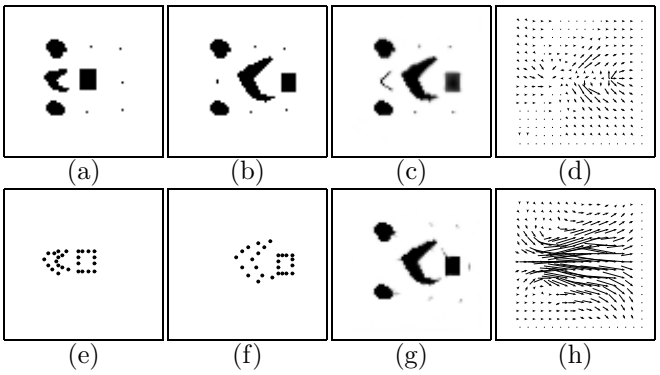

Figure 2: Comparison of synthetic multi-object image (64 × 64) non-rigid registration. (a): atlas image; (b): study image; (c): final fluidly deformed atlas by Christensen's fluid model [4]; (d): unreasonable vector map of the final viscous-fluid transformation by Christensen's fluid model: objects deform rather than shifting to match shape (compare to (h)); (e): atlas image control points; (f): study image control points; (g): final deformed atlas using our non-rigid registration method; (h): vector map of our final fluid transformation showing appropriate displacement of objects (compare to (d)).

and β are Lamé constants. The body force, $\vec{F}(\vec{u})$, is the driving function that deforms the atlas into the shape of the study, which will be formulated in detail in Section 4.

2.2 Fluid Model

For viscous fluids, the force is proportional to the time rate of change in displacement. The PDE describing the fluid transformation of the atlas is given by

$$\mu \bigtriangledown^2 \vec{v} + (\mu + \beta)\vec{\bigtriangledown}(\vec{\bigtriangledown} \cdot \vec{v}) = \vec{F}(\vec{u}) \tag{3}$$

where $\vec{v} = [v_x(\vec{w}, t), v_y(\vec{w}, t)]^T$ is the instantaneous velocity of the deformation field $\vec{u}$. It is related to its displacement, $\vec{u}$, by

$$\vec{v}(\vec{w}, t) = \frac{\partial \vec{u}(\vec{w}, t)}{\partial t} + \vec{v}(\vec{w}, t)^T \vec{\bigtriangledown} \vec{u}(\vec{w}, t) \tag{4}$$

The $\bigtriangledown^2 \vec{v}$ term is called the viscous term of the PDE. This term constrains neighboring particles of the displacement field to deform with roughly the same velocity by spatially smoothing the velocity field. The term $\vec{\bigtriangledown}(\vec{\bigtriangledown} \cdot \vec{v})$ is called the mass source term and it allows structures in the atlas to grow and shrink in mass. The coefficients μ and β are the viscosity coefficients. For the work herein, the boundary conditions are $\vec{v}(\vec{w}) = 0$ for $\vec{w}$ on the image boundary. The term $\vec{v}(\vec{x}, t)^T \vec{\bigtriangledown} \vec{u}(\vec{x}, t)$ accounts for nonlinear trajectories of particles as they pass through the observation points.

2.3 Viscous Fluid vs. Linear Elasticity

Eq.(3) is almost identical in form to Eq.(2) except that the displacement field $\vec{u}$ is replaced by the velocity field $\vec{v}$. However, these equations are very different, as can be seen by substituting Eq.(4) into Eq.(3). The nonlinear relationship between $\vec{v}$ and $\vec{u}$ expressed by Eq.(4) allows the fluid model to track long-distance, nonlinear deformations of small subregions.

The linear elastic model is derived assuming small angles of rotation and small linear deformations. Large deformations can not be accommodated with this linear PDE. However, even though linear elasticity does not guarantee a homeomorphic transformation, in practice a homeomorphic transformation can be generated using strong elasticity (large μ). The trade-off is that only small deformations can be generated [4]. This shortcoming of linear elasticity is removed by using the viscous model because the restoring forces relax over time and then account for the large-distance kinematic nonlinearities, while ensuring a homeomorphic transformation (globally positive Jacobian).

3 Statistical Shape Information

We have developed a statistical shape model based boundary finding with correspondence algorithm, which has been described in detail [12]. Global shape parameters derived from the statistical variation of object boundary points in a training set are used to model the object [5]. A Bayesian formulation, based on this prior knowledge and the edge information of the input image, is employed to find the object boundary with its subset points in correspondence with the point sets of boundaries in the training set.

Given m aligned examples, and for each example, a set of N labeled points, $\mathbf{L}_i$=($x_i(1)$,$y_i(1)$,$x_i(2)$,$y_i(2)$,$\cdots$, $x_i(N)$,$y_i(N)$)^T, $(i = 1, 2, \cdots, m)$, we calculate the mean shape, $\bar{\mathbf{L}}$, and the covariance about the mean, $C_{training}$. The t eigenvectors $\mathbf{q}_i$ of $C_{training}$ corresponding to the largest t eigenvalues, λ_i, give a set of uncorrelated basis vectors, or *modes of variation*, for a deformable model. A new example can be calculated using $\mathbf{L} = \bar{\mathbf{L}} + Q\mathbf{a}$, where $Q = (\mathbf{q}_1|\mathbf{q}_2|\cdots|\mathbf{q}_t)$ is the matrix of eigenvectors and $\mathbf{a} = (a_1, a_2, \cdots, a_t)^T$ is the vector of weights, or shape parameters, to be determined. As $\mathbf{a}$ varies from zero, the corresponding shapes will be similar to those in the training set.

Given the statistical models, our aim is to match them to particular examples of structure in the individual images, and find the parameter vector $\mathbf{p}$ consisting of the shape parameter, $\mathbf{a}$, and the pose parameters: scale s, rotation θ, and translation T_x, T_y.

A Bayesian formulation leads to ([12]):

$$M(\mathbf{p}) = \sum_{j=1}^{t+4} \left[-\frac{(p_j - m_j)^2}{2\sigma_j^2} \right] + \frac{1}{\sigma_n^2} \sum_{n=1}^{N} E(x(\mathbf{p}, n), y(\mathbf{p}, n)) \tag{5}$$

where m_j is the mean of p_j; σ_j is the standard deviation for each of the parameters; E is the edge image intensity of the input image and σ_n is the standard deviation of the white zero mean Gaussian noise associated with the image noise model [12]. This equation is the maximum *a posteriori* objective incorporating a prior bias to likely shapes and poses (first term) and a match to edges in the image (second term).

4 Integration

While physical models are useful in non-rigid registration, they are limited by themselves because they are too generic. Instead, the statistics of a sample of images can be used to guide the deformation in a way governed by the measured variation of individuals. Thus, this paper proposes algorithms which uses physical models, yet incorporates a statistical shape model to constrain solutions to more anatomically consistent deformations.

We pose the displacement estimation problem in a maximum *a posteriori* framework. As input to the problem, we have both the intensity image of the study (individual), $I_s(\vec{w})$, and the boundary points of the study $\vec{b_s}(\mathbf{p}, n) = (x_s(\mathbf{p}, n), y_s(\mathbf{p}, n))$, for $n = 1, 2, \cdots, N$, given the shape and pose parameters, $\mathbf{p}$, which are derived from the statistical shape model

based boundary finding [12]. Thus, we want to maximize:

$$\Pr(\vec{u}|I_s, \vec{b}_s(\mathbf{p})) = \frac{\Pr(\vec{u}, I_s, \vec{b}_s(\mathbf{p}))}{\Pr(I_s, \vec{b}_s(\mathbf{p}))} \quad (6)$$

Ignoring the denominator, which does not change with $\vec{u}$, and by using Bayes rule, our aim is to find:

$$\begin{aligned} &\arg\max_{\vec{u}} \Pr(\vec{u}|I_s, \vec{b}_s(\mathbf{p})) \\ &\equiv \quad \arg\max_{\vec{u}} \Pr(\vec{b}_s(\mathbf{p})|\vec{u}, I_s) \Pr(I_s|\vec{u}) \Pr(\vec{u}) \\ &\propto \arg\max_{\vec{u}} \left[\ln \Pr(\vec{u}) + \ln \Pr(I_s|\vec{u}) + \ln \Pr(\vec{b}_s(\mathbf{p})|\vec{u})\right] \end{aligned} \quad (7)$$

where we ignore the dependence of $\vec{b}_s(\mathbf{p})$ on I_s because $\vec{b}_s(\mathbf{p})$ is obtained as a prior here and is not modified in this formulation, and take the logarithm.

The Bayesian posterior can be connected to the PDE for physical models based on a variational principle [4, 10]. The forcing function in the PDEs (Eq.(2) and Eq.(3)) is the variation of the likelihood function with respect to the vector displacement field [1, 8].

The first term in Eq.(7) corresponds to the transformation prior term, which gives high probability to transformations consistent with a physical model (elastic solid or viscous fluid) and low probability to all other transformations. As mentioned above, they are given by Eq.(2) for the elastic model, and Eqs.(3) &(4) for the fluid model.

The second term in Eq.(7) is actually the likelihood term which depends on the study image. Let $I_a(\vec{w})$ be the intensity image of the atlas. We model the study image as a Gaussian process with mean given by the deformed atlas image, $I_a(\vec{w}-u(\vec{w}))$ [4] (since an Eulerian reference frame is used here, a mass particle instantaneously located at $\vec{w}$ originated from point $\vec{w}-\vec{u}(\vec{w})$). That is,

$$\ln \Pr(I_s|\vec{u}) = -\frac{1}{2\sigma_1^2} \int_\Omega \left[I_s(\vec{w}) - I_a(\vec{w} - u(\vec{w}))\right]^2 d\vec{w}$$

where σ_1 is the standard deviation of the Gaussian process.

The first body force, $\vec{F}_1$, is the gradient of this likelihood term with respect to $\vec{u}$ at each $\vec{w}$ [4]:

$$\vec{F}_1(\vec{u}) = -\frac{1}{\sigma_1^2} \left[I_s(\vec{w}) - I_a(\vec{w} - u(\vec{w}))\right] \nabla I_a(\vec{w} - u(\vec{w})) \quad (8)$$

The main contribution of this paper lies in the last term of Eq.(7), which incorporates statistical shape information into the non-rigid registration framework. The extra constraint of corresponding boundary points is used as an additional matching criterion. The boundary point positions are the result of the deformation of the model to fit the data in ways consistent with the statistical shape models derived from the training set, as described in Section 3. Let $\vec{b}_a(n) = (x_a(n), y_a(n))$, for $n = 1, 2, \cdots, N$, denote the atlas boundary points positions, which are known since we have full information about the atlas. We now model $\vec{b}_s(\mathbf{p})$ as a Gaussian process with mean given by the deformed atlas boundary position, expressed as $\vec{b}_a(n)+\vec{u}(\vec{w})$, for pixels $\vec{w}$ on the deformed atlas boundary points. Then,

$$\ln \Pr(\vec{b}_s(\mathbf{p})|\vec{u}) = -\frac{1}{2\sigma_2^2} \sum_{n=1}^{N} ||\vec{b}_s(\mathbf{p}, n) - \left[\vec{b}_a(n) + \vec{u}(\vec{w})\right]||^2$$

where σ_2 is again the standard deviation of the Gaussian process.

The second body force, $\vec{F}_2$, is then the gradient of the above equation with respect to $\vec{u}$ for pixels $\vec{w}$ on the deformed atlas boundary points:

$$\vec{F}_2(\vec{u}) = \frac{1}{\sigma_2^2} ||\vec{b}_s(\mathbf{p}, n) - \left[\vec{b}_a(n) + \vec{u}(\vec{w})\right]|| \quad (9)$$

$\vec{F}_2(\vec{u})$ is zero for pixels $\vec{w}$ not on the deformed atlas boundary points.

The total force term, $\vec{F}(\vec{u})$, in Eq.(2) and Eq.(3) is then the weighted sum of $\vec{F}_1(\vec{u})$ in Eq.(8) and $\vec{F}_2(\vec{u})$ in Eq.(9), that is, for each $\vec{w}$,

$$\vec{F}(\vec{u}) = c_1\vec{F}_1(\vec{u}) + c_2\vec{F}_2(\vec{u}) \quad (10)$$

Here, $\vec{F}_1(\vec{u})$ matches the intensity of the atlas and the study, while $\vec{F}_2(\vec{u})$ matches their shape features, such as high curvature points and important anatomical landmarks. The two coefficients, c_1 and c_2, can be related to the image contrast and the deformation between the atlas and study image. For the time being, they are fixed empirically so that $\vec{F}_1(\vec{u})$ and $\vec{F}_2(\vec{u})$ are of the same order.

Our approaches that incorporate statistical shape information are then composed of Eq.(10) and Eq.(2) for the elastic model, and Eq.(10), Eq.(3) and Eq.(4) for the fluid model. In order to solve the problem, we discretize these equations and employ Euler integration in time (Eq.(4)) combined with successive over-relaxation (SOR) in the spatial domain (Eq.(2) and Eq.(3)).

5 Experimental Results

For all of the experiments, we apply either Christensen&Miller's elastic registration [8, 3] or Christensen's fluid registration [4] for a direct comparison based on our own implementation. As to the computation time, while our method requires an extra force ($\vec{F}_2$) calculation at sparse boundary points, this leads to faster and more accurate convergence. Also, since the boundary finding step takes only several seconds,

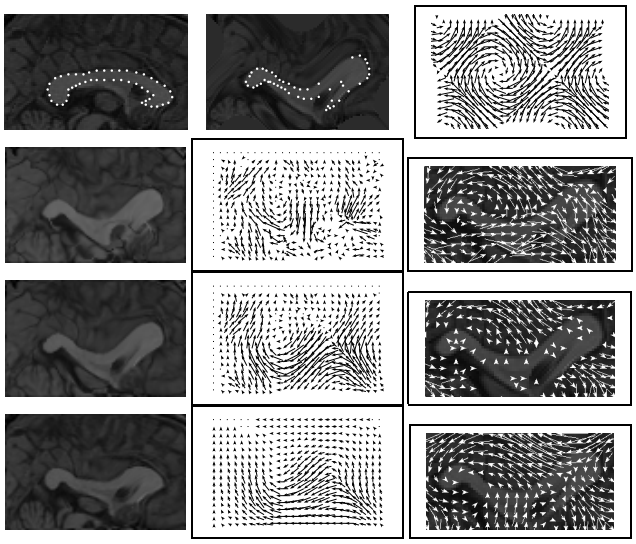

Figure 3: MR sagittal corpus callosum image (100×64) and synthetic displacement vectors. Top left: atlas image with control points; Top middle: study image with control points; Top right: true displacement vectors; From the second row to the bottom: The left column shows the deformed atlas by Christensen's fluid method (the second row), our fluid method (the third row), and our elastic method (bottom); The middle column shows the corresponding estimated vectors; The right column shows the corresponding errors in estimated vectors on the study image (cropped).

the total convergence times of our elastic and fluid methods are usually a little faster than or similar to Christensen's elastic and fluid methods, respectively. In general, the elastic methods take much less time than the fluid methods since no time integration is needed[1]. A comparison of the different methods' approximate execution time on a Silicon Graphics Octane 250-MHZ MIPS R10000 is also listed in Table 2.

In addition to the illustration of the previous synthetic image non-rigid registration examples (Figures 1 and 2), we also give the following validation of our methods. Previously, a demonstration of the sensitivity to noise for our and Christensen&Miller's elastic methods has been shown [13].

5.1 Images with Known Warping

For testing purposes, we can define a particular warp and apply it to a magnetic resonance (MR) sagittal brain image showing the corpus callosum (Figure 3 top left). A warped study image (Figure 3 top middle) is then generated based on the predetermined displacement vectors. We use a sinusoidal displacement field

[1]A detailed investigation of execution time for Christensen's elastic and fluid model on different computers can be found in [3].

Method	E_{oa} (%)	E_{om}	E_{ba} (%)
Christensen's fluid method	5.82 pixels (63.2%)	13.82 pixels	5.91 pixels (65.0%)
Our fluid method	0.99 pixels (11.4%)	2.29 pixels	0.89 pixels (9.8%)
Our elastic method	3.46 pixels (37.6%)	10.54 pixels	3.32 pixels (36.5%)

Table 1: Error measure for MR sagittal corpus callosum image with known warping. E_{oa}: average displacement error over corpus callosum; E_{om}: maximum displacement error over corpus callosum; E_{ba}: average displacement error on sparse boundary points. Note: the percentages shown with each average error are with respect to the true average displacement.

for transforming the atlas image to the study image (Figure 3 top right). To evaluate the methodology, we quantify errors in the displacement field over the objects of interest, since warping of the background is irrelevant. The average (E_{oa}) and maximum (E_{om}) differences between the estimated and actual displacement vectors over the objects are used to measure accuracy. We also use the average difference between the estimated and actual displacement vectors on the sparse boundary control points, E_{ba}. Since the control points are also derived from the known warp, all three measures only reflect the non-rigid registration, and do not include the boundary finding step.

Because the deformation here between the atlas and study is quite large, we use our fluid method to register the atlas image to the study image. For comparison, we also register the two images using Christensen's fluid method and our elastic method by choosing the appropriate elasticity parameter so that a homeomorphic map is just ensured (globally positive Jacobian). The results (Figure 3 and Table 1) show that our fluid method leads to a much better registration in the object of interest than Christensen&Miller's fluid method, and our elastic method because of the large deformation of the images which can not be tracked by the elastic model. Using our elastic method, the atlas can not deform well (Figure 3 bottom left).

5.2 Real Atlas and Study Images

Results of the method applied to MR brain (axial) and heart image pairs are shown in Figures 4 and 5. These are 2D slices that roughly correspond from different brains and hearts for demonstration purposes. Here, we only use the average difference between the estimated and actual displacement vectors on the sparse boundary control points, E_{ba}, as an accuracy measure because we do not know the true warp, except at sparse boundary points determined by an expert. Since the study image boundary control points are derived by our

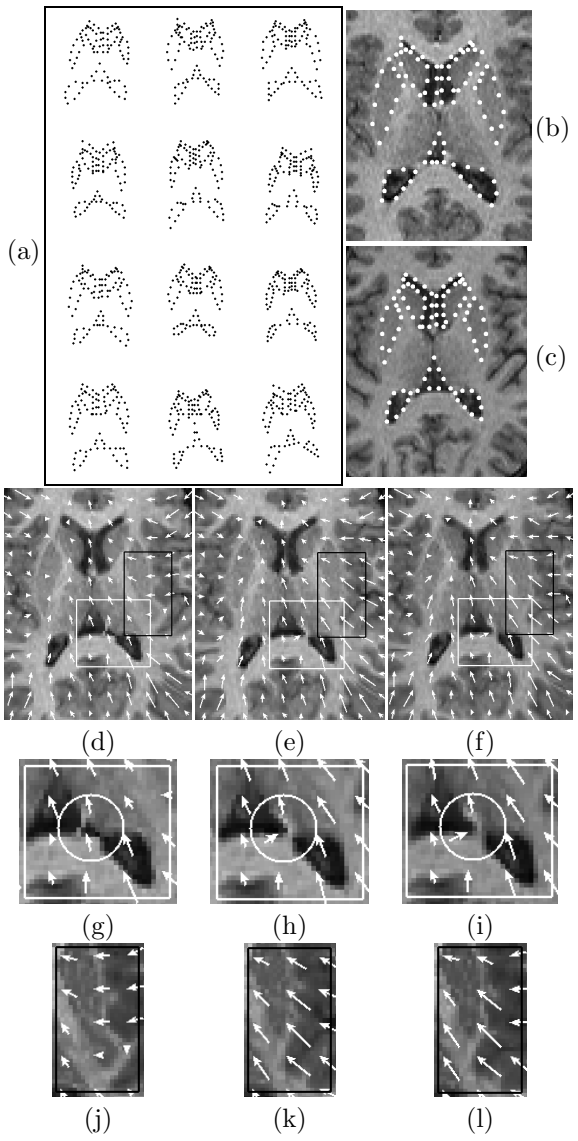

Figure 4: MR axial brain images (80 × 100), shape model and displacement vectors. (a): 12 examples of brain shapes from a training set with each example a 93 point model of basal ganglia and ventricle boundaries; (b): atlas image with its control points; (c): study image with its control points derived from our boundary finding algorithm [12]; (d): estimated vectors by Christensen&Miller's elastic method over their deformed atlas; (e): our elastically estimated vectors over our elastically deformed atlas; (f): our fluidly estimated vectors over our fluidly deformed atlas; (g): enlargement of (d) showing mis-matching due to Christensen&Miller's elastic method; (h): correct mapping of the ventricle corners by our elastic method; (i): correct mapping of the ventricle corners by our fluid method; (j): poorly deformed putamen by Christensen&Miller's elastic method (cropped); (k): well deformed putamen by our elastic method; (l): well deformed putamen by our fluid method.

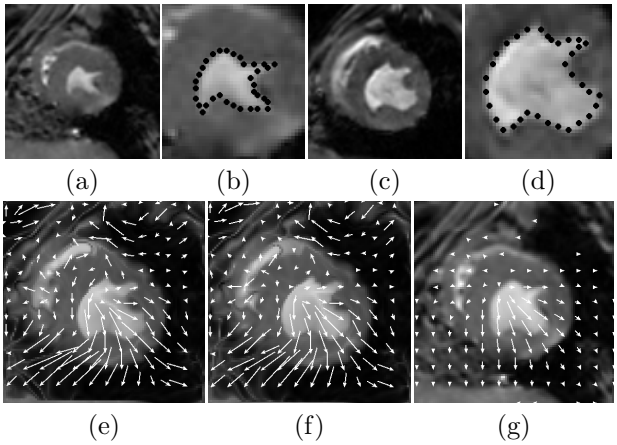

Figure 5: MR heart images (100 × 100) and displacement vectors. (a): atlas image; (b): atlas image with its control points on the endocardium (cropped); (c): study image; (d): study image with control points derived from our boundary finding algorithm; (e): estimated vectors by Christensen's fluid method over deformed atlas; (f): vectors by our fluid method over fluidly deformed atlas; (g): vectors by our elastic method over elastically deformed atlas (appropriate elasticity parameter is used to just ensure globally positive Jacobian).

Image	*Method*	E_{ba} (%)	time
Figure 4 Brain (80×100) with 93 control points	Christensen&Miller's elastic method	2.04 pixels (43.7%)	15 minutes
	Our elastic method	0.75 pixels (16.0%)	13 minutes
	Our fluid method	0.76 pixels (16.3%)	28 minutes
Figure 5 Heart (100×100) with 34 control points	Christensen's fluid method	2.08 pixels (28.7%)	60 minutes
	Our fluid method	0.92 pixels (12.6%)	60 minutes
	Our elastic method	1.92 pixels (26.4%)	5 minutes[2]

Table 2: Error measure E_{ba} and approximate execution time (Silicon Graphics Octane 250-MHZ MIPS R10000) for MR brain (axial) and heart images. E_{ba}: average displacement error on sparse boundary points. Note: the percentages shown with each average error are with respect to the true average displacement.

statistical shape model based boundary finding [12], the error, E_{ba}, for true image pairs includes both the boundary finding step and the non-rigid registration step. From the error measures shown in Table 2, we see that even with the error in the boundary find-

[2]The extremely short execution time for the heart images with our elastic method is due to pre-mature convergence.

ing step, the final error of our methods is still much better than Christensen's methods. Specifically, for brain images, the final error of our elastic and fluid methods perform similarly because for small deformations both of our methods work well, and much better than Christensen&Miller's elastic method. Note in particular in Figure 4, the corner of the third ventricle in the study was not registered to the atlas correctly by Christensen&Miller's elastic method (Figure 4(g)). The structures of the study are shifted away from the corresponding ones in the atlas based on gray level information. Our methods calculated the correct mapping (Figures 4(h) and 4(i)) by incorporating statistical shape information and using the corresponding boundary points as an extra constraint. Also note that the putamen did not deform well in Christensen&Miller's elastic method (Figure 4(j)) because the contrast of the putamen is too low compared to the contrast of the ventricles. In our approaches, the putamen deformed correctly (Figures 4(k) and 4(l)) since shape information of the putamen was included. For heart images, because of the large deformation, our fluid model works better than our elastic model, by which the atlas can not deform well (Figure 5(g)). More importantly, our fluid method results in much smaller error than Christensen's fluid method because of the included statistical shape information.

6 Conclusions

This work presents two systematic approaches for non-rigid registration. Transformations are constrained to be consistent with physical deformations of elastic solids in the first approach and viscous fluids in the second approach in order to maintain the topology, or integrity, of the anatomic structures while having high spatial dimension to accommodate complex anatomical details. Both intensity information and statistical shape information are used as matching criteria in a Bayesian formulation. The incorporation of statistical shape information into the framework is the main contribution of our work. From the experimental results, statistical boundary shape information has been shown to augment physical model formulations for non-rigid registration, and both of our methods have their own advantages under different situations.

Although we have only shown 2D formulations and results, the extension of our methods to the 3D case is straightforward. Of course, the computational cost increases with the number of voxels. Also, the coupling of boundary finding and registration can be increased by enabling registration to influence boundary finding, and thus both processes will enhance each other.

Acknowledgments

This work was supported in part by a grant from the Whitaker Foundation.

References

[1] Y. Amit, U. Grenander and M. Piccioni, "Structural image restoration through deformable templates," *J. American Statistical Association*, Vol. 86, no. 414, pp. 376-387, June 1991.

[2] F. L. Bookstein, "Shape and information in medical images: A decade of the morphometric synthesis," *Proc. Workshop Math. Meth. Biomed. Image Anal.*, pp. 2-12, June 1996.

[3] G. E. Christensen, M. I. Miller and M. W. Vannier, "Individualizing neuroanatomical atlases using a massively parallel computer," *Computer*, pp. 32-38, January 1996.

[4] G. E. Christensen, R. D. Rabbitt and M. I. Miller, "Deformable templates using large deformation kinematics," *IEEE Trans. on Image Processing*, Vol. 5, no. 10, pp. 1435-1447, October 1996.

[5] T. F. Cootes, C. J. Taylor, D. H. Cooper and J. Graham, "Active shape models – their training and application," *Computer Vision and Image Understanding*, Vol. 61, no. 1, pp. 38-59, 1995.

[6] C. Davatzikos and J. Prince, "Brain image registration based on curve mapping," *IEEE Workshop Biomedical Image Anal.*, pp. 245-254, 1994.

[7] J. Gee, L. L. Briquer, C. Barillot and D. Haynor, "Probabilistic matching of brain images," *Information Processing in Medical Imaging*, pp. 113-125, 1995.

[8] M. I. Miller, G. E. Christensen, Y. Amit and U. Grenander, "Mathematical textbook of deformable neuroanatomies," *Proc. National Academy of Science*, Vol. 90, no. 24, pp. 11944-11948, 1993.

[9] R. D. Rabbitt, G. E. Christensen and M. I. Miller, "Mapping of hyperelastic deformable templates using finite element method," *Vision Geometry IV*, Vol. 2573, pp. 252-265, July 1995.

[10] J. N. Reddy, *Energy and Variational Methods in Applied Mechanics*, New York: Wiley-Interscience, 1984.

[11] J. P. Thirion, "Non-rigid matching using demons," *Proc. Conf. Computer Vision and Pattern Recognition*, pp. 245-251, June 1996.

[12] Y. Wang and L. H. Staib, "Boundary finding with correspondence using statistical shape models," *Proc. Conf. Computer Vision and Pattern Recognition*, pp. 338-345, Santa Barbara, California, June 1998.

[13] Y. Wang and L. H. Staib, "Elastic model based non-rigid registration incorporating statistical shape information," *First Int. Conf. on Medical Image Computing and Computer-Assisted Intervention*, in press, Cambridge, Massachusetts, October, 1998.